Inelastic Mach-Zehnder Interferometry with Free Electrons

Cameron W. Johnson,[1] Amy E. Turner,[1] F. Javier García de Abajo,[2,3] and Benjamin J. McMorran[1,*]
[1]Department of Physics, University of Oregon, Eugene, Oregon 97403, USA
[2]ICFO-Institut de Ciencies Fotoniques, Mediterranean Technology Park, 08860 Castelldefels (Barcelona), Spain
[3]ICREA-Institució Catalana de Recerca i Estudis Avançats, Passeig Lluís Companys 23, 08010 Barcelona, Spain

(Received 17 October 2021; accepted 9 March 2022; published 8 April 2022)

We use a novel scanning electron Mach-Zehnder interferometer constructed in a conventional transmission electron microscope to perform inelastic interferometric imaging with free electrons. An electron wave function is prepared in two paths that pass on opposite sides of a gold nanoparticle, where plasmons are excited before the paths are recombined to produce electron interference. We show that the measured spectra are consistent with theoretical predictions, specifically that the interference signal formed by inelastically scattered electrons is π out of phase with respect to that formed by elastically scattered electrons. This technique is sensitive to the phase of localized optical modes, because the interference signal amounts to a substantial fraction of the transmitted electrons. Thus, we argue that inelastic interferometric imaging with our scanning electron Mach-Zehnder interferometer provides a new platform for controlling the transverse momentum of free electrons and studying coherent electron-matter interactions at the nanoscale.

DOI: 10.1103/PhysRevLett.128.147401

Introduction.—Free electrons in transmission electron microscopes (TEMs) are ideal for probing individual nanoplasmonic systems [1]. They couple to electromagnetic fields and form spectrally resolved high-resolution images via electron energy-loss spectroscopy (EELS), which is sensitive to the intensity of the probed optical fields but insensitive to their phase [1]. In general, scattered free electrons are viable quantum probes for characterizing nanoplasmonic systems [2], but access to mode phase requires manipulation of the electron wave function. Here, we explore the relationship between the phase of both free electrons and the plasmons they generate by introducing a new interferometric technique uniquely capable of exploring transverse spatial correlations between free electrons and condensed-matter excitations.

Several experiments in TEMs have exploited this phase coherence associated with inelastic electron-matter interactions. In particular, inelastic holography relies on an electrostatic biprism to interfere different parts of an electron wave after interacting with the sample and has been used to measure the coherence properties of bulk and surface plasmon excitations [3,4], as well as the loss of coherence due to the electromagnetic interaction with thermally populated material excitations [5]. However, a partial degree of electron source coherence and the production of multiple final states after electron-sample interaction complicate the analysis and interpretation of measured signals [6–8]. Likewise, shaping the electron wave front to match the spatial distribution of the probed plasmonic near field followed by postselection of the scattered electrons has been demonstrated as a method to filter localized plasmon resonances (LPRs) of dipolar or quadrupolar character in a metallic nanorod [9]. This method was also proposed to measure the transfer of orbital angular momentum [10], although postselecting wave fronts is inefficient and requires precise alignments in the mode matching and selection apertures, thus prohibiting concurrent high-quality imaging. Several theoretical [11–13] and experimental [14] works have addressed sorting of free electrons into different measurement bases, but actual realizations have a limited scope so far. Alternatively, the combination of pulsed lasers and synchronized electrons has been used to resolve nanoscale optical fields [15–18], but this approach requires highly specialized TEMs and ultrafast optical systems.

In this Letter, we use a two-grating electron Mach-Zehnder interferometer (2GeMZI) that produces two, spatially separated interaction probes (the ± 1 diffraction orders of the first grating) to image the interference of coherent superpositions of electrons inelastically scattered by the induced LPR excitations of an individual gold nanoparticle (NP). After interaction with the sample, the probes pass through a second grating, recombining the separate paths for copropagation to a detector and, therefore, allowing for complete interference in the interferometer output (see more details in Ref. [19]). The latter is collected by an EELS system to spectrally resolve the plasmon-scattered electrons from the zero-loss peak (ZLP) (Fig. 1). The interference of the inelastic signal as a function of the interferometer phase demonstrates that electrons in a coherent superposition of different paths can interact inelastically with the sample and remain

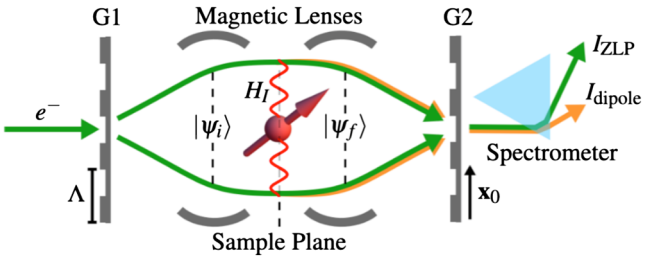

FIG. 1. Illustration of experiment. An electron is split by a grating ($G1$) with pitch $\Lambda = 2\pi/|\mathbf{k}_0|$, preparing it in the superposition state $|\psi_i\rangle$. The separated paths are focused and steered by magnetic lenses to interact with the dipolar plasmon of a gold nanoparticle (interaction Hamiltonian H_I) producing the final state $|\psi_f\rangle$. The paths are recombined using a second grating ($G2$ with the same pitch Λ) that is continuously translatable by $\mathbf{x}_0$. The position $\mathbf{x}_0$ of $G2$ tunes the relative path phase in the interferometer output as $\Delta\phi_{\text{int}} = 2\mathbf{k}_0 \cdot \mathbf{x}_0$. The output of the interferometer is dispersed in a spectrometer to resolve the elastic ZLP (green) and an inelastic peak corresponding to excitation of a dipolar plasmon (orange).

coherent after transmission through the interferometer. The robust 2GeMZI described in this Letter has the ability to scan spatially separated paths, tune the relative probe phase, and create discrete, copropagating outputs, opening the door to a diverse range of electron-wave-based experiments that were not possible before.

Dipolar interactions in the 2GeMZI.—The 2GeMZI separates the electron wave function into two parts, as depicted in Fig. 1. The incident electron state $|\psi_i\rangle$ is prepared such that there are two focal spots at the sample plane that are physically created using the first grating ($G1$). The final state of the electron $|\psi_f\rangle$ is postselected after interacting with the sample by means of a second grating ($G2$) combined with the entrance aperture of the electron energy analyzer. Near the sample plane, we can write the real-space representation of the incident electron wave function as $\psi_i(\mathbf{r}) = \langle \mathbf{r}|\psi_i\rangle = [\chi_i(\mathbf{r}-\mathbf{r}_1) + e^{i\phi_i}\chi_i(\mathbf{r}-\mathbf{r}_2)]/\sqrt{2}$, where χ_i is a normalized function describing each of the two nonoverlapping spots (centered at positions $\mathbf{r}_1$ and $\mathbf{r}_2$, respectively) and ϕ_i is a relative phase shift produced by stray potentials or any other differences between the two electron paths, such as the alignment of $G1$ relative to the optical axis (see below). Ignoring off-axis diffracted beams after $G2$, the state $|\psi_f\rangle$ takes the same functional form as the time reversal of $|\psi_i\rangle$ (i.e., it can be regarded as the mirror image of $|\psi_i\rangle$ through the sample plane, but with the electron traveling backward). Consequently, we can write $\psi_f(\mathbf{r}) = \langle \mathbf{r}|\psi_f\rangle = [\chi_f(\mathbf{r}-\mathbf{r}_1) + e^{i\phi_f}\chi_f(\mathbf{r}-\mathbf{r}_2)]/\sqrt{2}$. Additionally, for a lateral displacement $\mathbf{x}_0$ of $G1$ (or $G2$) along a direction across the grooves, we have that ϕ_i (or ϕ_f) is modified by a term $\Delta\phi_{\text{int}} = 2\mathbf{k}_0 \cdot \mathbf{x}_0$, where $|\mathbf{k}_0| = 2\pi/\Lambda$ is the wave number of the gratings with pitch Λ. This term arises directly from the phase difference between the two first-order diffraction orders introduced by a translation of $G2$.

In the absence of a sample, the arguments above allow us to write the measured electron intensity output of the interferometer (i.e., the ZLP) as

$$I_{\text{ZLP}} \propto |\langle \psi_f|\psi_i\rangle|^2 \propto \cos^2(\Delta\phi/2), \tag{1}$$

where the total relative path phase $\Delta\phi = \Delta\phi_{\text{int}} + \Delta\phi_{\text{ext}}$ receives contributions from the interferometer alignment $\Delta\phi_{\text{int}}$ and the noted path-related phases $\Delta\phi_{\text{ext}} = \phi_f - \phi_i$. In contrast, when a sample is inserted, the inelastic signal becomes $\propto \sum_e |\langle \psi_f|\langle e|H_I|g\rangle|\psi_i\rangle|^2$, where H_I is the electron-sample interaction Hamiltonian, $|g\rangle$ represents the initial sample ground state, we sum incoherently over all final excited sample states $|e\rangle$, and each term in the sum may involve a different final electron energy. However, the electron wave function can still be approximated by $\psi_f(\mathbf{r})$ for each $|e\rangle$ (i.e., the energy loss does not significantly affect electron propagation, other than in the spectral separation performed at the analyzer [20]). For a dipolar sample excitation of transition dipole $\mathbf{p}$ placed at a position $\mathbf{r}_c = (\mathbf{r}_1 + \mathbf{r}_2)/2$ (the sample is centered between the two electron spots) and oriented along the interspot direction $\mathbf{r}_2 - \mathbf{r}_1$, we have $H_I(\mathbf{r}) \propto \mathbf{p} \cdot (\mathbf{r} - \mathbf{r}_c)$. So, for a small spot size compared to r_c, the inelastic signal becomes

$$I_{\text{dipole}} \propto \sin^2(\Delta\phi/2). \tag{2}$$

In general, for an excitation characterized by an angular momentum number m, we have $H_I(\mathbf{r}) \propto e^{im\varphi}$, where φ is the azimuthal angle relative to $\mathbf{r}_c$. Following the same procedure as above, the inelastic signal is $\propto \cos^2[(\Delta\phi + m\Delta\varphi)/2]$, where $\Delta\varphi = \varphi_2 - \varphi_1$ is the relative azimuthal angle between the two electron positions with respect to $\mathbf{r}_c$. By directly applying this analysis to each multipole of a spherical particle, and if the two spots are each at a radial distance R from the sphere's center, the inelastic plasmon 2GeMZI signal is

$$I_{\text{sphere}}(\Delta\phi) \propto \frac{e^2}{c\hbar\omega}\sum_{l=1}^{\infty}\sum_{m=-l}^{l} C_{lm}^{E}\,\text{Im}\{t_l^E(\omega)\}K_m^2\left(\frac{\omega R}{v\gamma}\right) \times \cos^2[(\Delta\phi + m\Delta\varphi)/2], \tag{3}$$

where C_{lm}^E are electric coupling coefficients, t_l^E are Mie scattering matrix elements, K_m are modified Bessel functions of the second kind, v is the electron velocity, γ is the relativistic Lorentz factor, and $\hbar\omega$ is the energy loss. In this expansion, we retain only electric modes (E) that dominate the response of the considered NP, and, in particular, the $l = 1$ terms stand for the dipolar excitations, with $|m| = 1$ corresponding to the sample-plane-oriented dipole and $m = 0$ denoting the along-the-beam dipole (see Supplemental Material [21]). Furthermore, we find it useful to define the interference part of the inelastic signal:

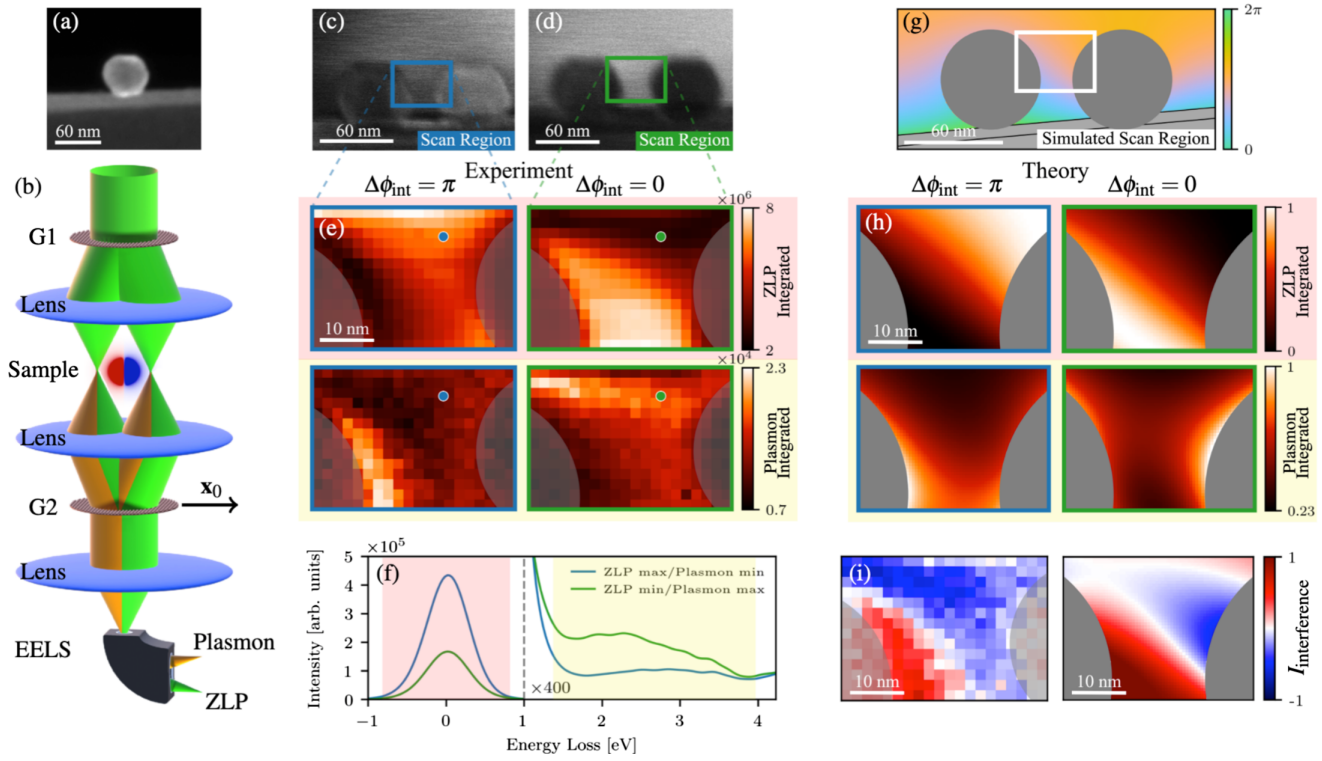

FIG. 2. Demonstration of inelastic interferometry. (a) Dark-field STEM image of a 60 nm gold NP on the edge of a carbon substrate. (b) Sketch of the 2GeMZI, consisting of a STEM with two gratings used as beam splitters. The first grating ($G1$) prepares electrons in a superposition of two separate paths, each of them interacting with the NP sample, with some probability of losing energy to a plasmon resonance (orange). (c),(d) The electron paths are recombined using the second grating ($G2$), which can be positioned for (c) destructive (blue borders) and (d) constructive (green borders) interference, conversely modifying the elastic and inelastic signals. Two NPs are observed in the image because of the two-spot beam configuration, with the central frame selecting the interference region (i.e., each beam passing by one side of the NP). (e),(f) For both alignment schemes, we integrate over the plasmon (yellow-shaded) and ZLP (red-shaded) regions of the energy-loss spectra plotted in (f) at every scan location to create the spectral images shown in (e). The raw spectra in (f) correspond to the dotted positions in (e). (g),(h) We simulate the experiment with an external potential $V_z(\mathbf{R})$ (g) and show that the calculated results (h) are qualitatively consistent with the experimental spectral images in (e). (i) Interference term of the loss probability, obtained as the difference of the plasmon-integrated spectral images from the two different interferometer alignments in (e) and (h) [Eq. (4)].

$$I_{\text{interference}} = I_{\text{sphere}}(\Delta\phi_{\text{int}} = 0) - I_{\text{sphere}}(\Delta\phi_{\text{int}} = \pi) \tag{4}$$

(see below).

We probe spherical NPs of ≈60 nm diameter and set a 80 nm path separation in the 2GeMZI [Figs. 2(a) and 2(b)]. With these parameters, the $l = 1$ dipole mode in Eq. (3) is dominant, while higher-order terms can be safely neglected (see Supplemental Material [21]). Additionally, we have recently shown that multiprobe imaging with the 2GeMZI induces sample charging that can cause significant relative phase shifts between the interferometer paths [19]. This external phase shift can be effectively modeled for the probes at transverse positions $\mathbf{R}_1$ and $\mathbf{R}_2$ passing through an electrostatic potential produced by the sample charging as $\Delta\phi_{\text{ext}} = \sigma[V_z(\mathbf{R}_2) - V_z(\mathbf{R}_1)]$, where $\sigma = e/\hbar v$ is the first-order interaction parameter and $V_z(\mathbf{R}) = \int dz V(\mathbf{r})$ is the projected potential [25] (see Supplemental Material [21]).

Description of the experiment.—The 2GeMZI was constructed in an image-corrected 80–300 keV FEI Titan TEM by placing the input grating $G1$ in the condenser aperture holder above the specimen plane and $G2$ in the selected area aperture holder below the specimen plane (see Ref. [19]). The TEM was operated at 80 keV, such that the STEM probe convergence angle was tunable from 1 to 10 mrad. Both binary diffraction gratings, $G1$ and $G2$, were milled into a 30-nm-thick freestanding Si_3N_4 membrane with 300 nm pitch and optimized to maximize intensity in the ± 1 diffraction orders while yielding a minimum in the zeroth order. Approximately 30% of the transmitted intensity was placed in each of the ± 1 orders and $< 6\%$ in any other order. A subsequent condenser aperture [19] limited the beam to a 3 mrad convergence angle. Then, a postspecimen lens was used to project a focused image of $G1$ onto $G2$. In addition, the post-$G2$ projection lenses were used to produce a real-space image of the interferometer output into the entrance aperture of the EELS system, yielding a ZLP of 0.8 eV full width at half maximum. In this

configuration, the scan and descan coils were used to raster the probes over a 200×200 nm^2 region in the specimen plane while maintaining the alignment of $G1$, $G2$, and the EELS aperture. The ± 1 diffraction-order probes were 5 nm wide and separated by 80 nm. Nevertheless, our demonstrated 2GeMZI can be applied to a wide range of sample sizes and beam-spot separations by suitably adjusting lens magnifications or grating placement and pitch.

Gold was chosen as a NP material for its resistance to form oxides, long-term stability, availability, and ease of sample preparation, although its LPRs overlap with interband transitions, in contrast to silver [26]. A monodisperse solution of gold NPs (60 nm diameter) was dropcast on a lacey carbon grid, dried in air, and placed in the TEM. A single NP was isolated on an edge of the carbon such that the two electron paths could pass on either side of the NP through vacuum [Figs. 2(a) and 2(b)], yielding $\Delta\varphi \approx \pi$ [Figs. 2(c) and 2(d)]. Then, spectral images were recorded for both destructive and constructive interferometer outputs [Fig. 2(e)] (see Supplemental Material [21]). Integration over the energy ranges $(-1, 1)$ eV for the ZLP and (1.5,4) eV for the plasmon peaks, as shown in Fig. 2(f), produced energy filtered spectral images [Fig. 2(e)].

Results and discussion.—Figure 2(a) shows that the carbon support has a much larger surface area than the NP and there is a small azimuthal tilt angle offset between the carbon edge and the horizontal diffraction direction of the scanning probes. Consequently, we model the contribution of the carbon edge to be 30 times stronger than that from the NP in the approximate external potential and further account for a 5° angular misalignment between the probes and the carbon edge [Fig. 2(g)]. We use this simulated potential to generate spectral images via Eq. (3) that are in excellent qualitative agreement with the experimental results [Fig. 2(h)]. By taking the difference of the plasmon-integrated spectral images with the destructive and constructive interferometer alignments, we can find the spatially resolved interference term in the energy-loss spectrum [Eq. (4)], which shows the same structure as the simulated result [Fig. 2(i)].

As a more quantitative visualization, we assign a relative probe phase to each pixel in Fig. 2(e) by normalizing the ZLP intensity and inverting Eq. (1). The normalized integrated ZLP and plasmon intensities of each pixel are plotted as a function of the assigned relative probe phase in Fig. 3. We show the mean values binned by every $\pi/12$ relative phase interval along with the theoretically predicted values for $\Delta\varphi = \pi$. To account for the uncertainty in the ZLP intensity maxima and minima corresponding to $\Delta\phi = 0$ and $\Delta\phi = \pi$, we introduce a $\pi/12$ systematic error in the standard deviation of the binned values added in quadrature. The error given for the mean integrated plasmon intensities is the standard deviation for each binned region, and the phase error is assumed to be the same as the mean ZLP data. Deviation of the measured ZLP intensity from the theoretical prediction is well understood by the small, but nonzero contributions of the higher-order probes from G1 causing a loss of fringe visibility. This does not have a substantial effect on the visibility of the plasmon interference, because the higher-order probes are further away from the NP than the main ± 1 probes and the plasmon loss probability is exponentially suppressed for large impact parameters [27]. Additional measurements were performed on a separate gold NP, also demonstrating the converse dipole interference relation (see Supplemental Material [21]).

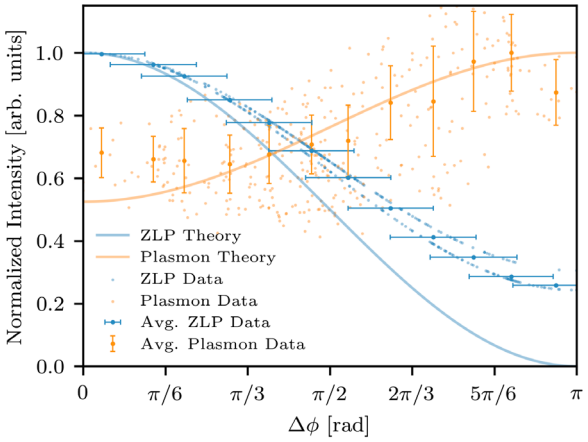

FIG. 3. Measured and modeled ZLP and plasmon intensities as a function of total relative probe phase.

Similar conditional interference relations exist between the ZLP and higher-order multipolar modes, dependent on the geometry and symmetry of their spatial distributions and the probe positions, although they are not spectrally resolvable in spherical gold NPs. However, multiple plasmon peaks are resolved in anisotropic NPs [28], NP assemblies [29], or NPs made of less lossy materials [30], where such relations could be explored using a 2GeMZI with improved spectral resolution. Integration of a cathodoluminescence collection system with a 2GeMZI could provide information about the correlation between the phase-coherent superpositions of scattered electrons and photons emitted from radiative dipole plasmon decay [31,32]. This 2GeMZI could also serve to measure the transfer of orbital angular momentum [11,12,14]. Finally, we note that inelastic free-electron interference in the 2GeMZI is not exclusive to plasmon scattering and can be used to probe polaritons and condensed-matter excitations, in general [33].

Conclusion.—We have demonstrated phase-sensitive interference between coherent superpositions of inelastically scattered free electrons within a two-probe 2GeMZI from plasmonic excitations of a single gold NP. The excitation of a plasmon introduces an expected relative π phase difference between the two interferometer paths of the inelastically scattered electrons, which is well described by a dipolar interaction. Isolating this interferometer output

provides a potential way to detect dipolar excitations at energies below the resolution of the microscope. Beyond individual modes, the present method should be capable of retrieving the relative complex amplitude of the nonlocal electromagnetic Green tensor associated with the optical response of a specimen. Additionally, the high throughput, flexibility, scanning capabilities, and ease of operation in a conventional scanning TEM of this technique provide an exciting platform for probing quantum mechanics at the nanoscale and allow for control over the transverse momentum of the free electron wave function. Further development of the present technique could lead to tests of quantum complementarity for free electrons [34], explorations of decoherence theory [35], and manipulation of free electrons with unprecedented versatility [2].

We thank Joshua Razink for the TEM instrument support. This work was supported by National Science Foundation (NSF) Grants No. 1607733 and No. 2012191. C. W. J. was supported by the NSF GRFP Grant No. 1309047. F. J. G. A. acknowledges support from the European Research Council (789104eNANO) and the Spanish MICINN (PID2020–112625 GB-I00 and SEV2015- 0522).

*mcmorran@uoregon.edu

[1] F. J. García de Abajo, Rev. Mod. Phys. **82**, 209 (2010).
[2] A. Polman, M. Kociak, and F. J. García de Abajo, Nat. Mater. **18**, 1158 (2019).
[3] H. Lichte and B. Freitag, Ultramicroscopy **81**, 177 (2000).
[4] F. Röder and H. Lichte, Eur. Phys. J. Appl. Phys. **54**, 33504 (2011).
[5] N. Kerker, R. Röpke, L. M. Steinert, A. Pooch, and A. Stibor, New J. Phys. **22**, 063039 (2020).
[6] S. L. Y. Chang, C. Dwyer, C. B. Boothroyd, and R. E. Dunin-Borkowski, Ultramicroscopy **151**, 37 (2015).
[7] J. Verbeeck, D. van Dyck, H. Lichte, P. Potapov, and P. Schattschneider, Ultramicroscopy **102**, 239 (2005).
[8] J. Verbeeck, Ultramicroscopy **106**, 461 (2006).
[9] G. Guzzinati, A. Béché, H. Lourenço-Martins, J. Martin, M. Kociak, and J. Verbeeck, Nat. Commun. **8**, 14999 (2017).
[10] D. Ugarte and C. Ducati, Phys. Rev. B **93**, 205418 (2016).
[11] A. Asenjo-Garcia and F. J. García de Abajo, Phys. Rev. Lett. **113**, 066102 (2014).
[12] M. Zanfrognini, E. Rotunno, S. Frabboni, A. Sit, E. Karimi, U. Hohenester, and V. Grillo, ACS Photonics **6**, 620 (2019).
[13] H. Lourenço-Martins, D. Gérard, and M. Kociak, Nat. Phys. **17**, 598 (2021).
[14] A. H. Tavabi, P. Rosi, E. Rotunno, A. Roncaglia, L. Belsito, S. Frabboni, G. Pozzi, G. C. Gazzadi, P.-H. Lu, R. Nijland, M. Ghosh, P. Tiemeijer, E. Karimi, R. E. Dunin-Borkowski, and V. Grillo, Phys. Rev. Lett. **126**, 094802 (2021).
[15] B. Barwick, D. J. Flannigan, and A. H. Zewail, Nature (London) **462**, 902 (2009).
[16] T. T. A. Lummen, R. J. Lamb, G. Berruto, T. LaGrange, L. Dal Negro, F. J. García de Abajo, D. McGrouther, B. Barwick, and F. Carbone, Nat. Commun. **7**, 13156 (2016).
[17] L. Piazza, T. T. A. Lummen, E. Quiñonez, Y. Murooka, B. W. Reed, B. Barwick, and F. Carbone, Nat. Commun. **6**, 6407 (2015).
[18] A. Feist, K. E. Echternkamp, J. Schauss, S. V. Yalunin, S. Schäfer, and C. Ropers, Nature (London) **521**, 200 (2015).
[19] C. W. Johnson, A. E. Turner, and B. J. McMorran, Phys. Rev. Research **3**, 043009 (2021).
[20] J. Krehl, G. Guzzinati, J. Schultz, P. Potapov, D. Pohl, J. Martin, J. Verbeeck, A. Fery, B. Büchner, and A. Lubk, Nat. Commun. **9**, 4207 (2018).
[21] See Supplemental Materials at http://link.aps.org/supplemental/10.1103/PhysRevLett.128.147401 for a detailed derivation of Eq. (3), a discussion of the form of the charging potential, data collection and processing methods, and additional experimental data, which includes Refs. [22–24].
[22] P. B. Johnson and R. W. Christy, Phys. Rev. B **6**, 4370 (1972).
[23] F. J. García de Abajo, Phys. Rev. B **59**, 3095 (1999).
[24] J. Nelayah, M. Kociak, O. Stéphan, F. J. García de Abajo, M. Tencé, L. Henrard, D. Taverna, I. Pastoriza-Santos, L. M. Liz-Marzán, and C. Colliex, Nat. Phys. **3**, 348 (2007).
[25] J. M. Cowley and S. Iijima, Z. Naturforsch. **27A**, 445 (1972).
[26] V. Amendola, R. Pilot, M. Frasconi, O. M. Maragò, and M. A. Iatì, J. Phys. Condens. Matter **29**, 203002 (2017).
[27] In other words, $K_m(x) \sim e^{-x}\sqrt{\pi/2x}$ for large x.
[28] M. Bosman, V. J. Keast, M. Watanabe, A. I. Maaroof, and M. B. Cortie, Nanotechnology **18**, 165505 (2007).
[29] S. J. Barrow, D. Rossouw, A. M. Funston, G. A. Botton, and P. Mulvaney, Nano Lett. **14**, 3799 (2014).
[30] L. Kiewidt, M. Karamehmedović, C. Matyssek, W. Hergert, L. Mädler, and T. Wriedt, Ultramicroscopy **133**, 101 (2013).
[31] N. Yamamoto, K. Araya, and F. J. García de Abajo, Phys. Rev. B **64**, 205419 (2001).
[32] M. Kociak and L. F. Zagonel, Ultramicroscopy **176**, 112 (2017).
[33] N. Rivera and I. Kaminer, Nat. Rev. Phys. **2**, 538 (2020).
[34] M. O. Scully, B.-G. Englert, and H. Walther, Nature (London) **351**, 111 (1991).
[35] P. Schattschneider and S. Löffler, Ultramicroscopy **190**, 39 (2018).